Separation and Purification Technology 406 (2026) 138996

Contents lists available at ScienceDirect

Separation and Purification Technology

journal homepage: www.elsevier.com/locate/seppur

Mechanistic evaluation of chitosan and aluminum chlorohydrate pre-coagulation for fouling mitigation during ultrafiltration of wildfire-affected soil leachate

Sohail Farooq [a], Ryan P. Cole [b], Amanda K. Hohner [c], Kevin D. Bladon [b,d], Xue Jin [a,*]

[a] School of Chemical, Biological, and Environmental Engineering, Oregon State University, Corvallis, OR 97331, USA
[b] Department of Forest Engineering, Resources, and Management, Oregon State University, Corvallis, OR, USA
[c] Department of Civil Engineering, Montana State University, Bozeman, MT, USA
[d] Department of Forest Ecosystems and Society, Oregon State University, Corvallis, OR, USA

ARTICLE INFO

Keywords:
Wildfire
Water quality
Coagulation
Chitosan
Ultrafiltration
Membrane fouling

ABSTRACT

Wildfires can impair source water quality by increasing turbidity, dissolved organic matter (DOM), nutrients, and disinfection by-product precursor loading, creating challenges for membrane-based drinking water treatment. In this study, aluminum chlorohydrate (ACH) and chitosan were compared as pre-coagulants for inline coagulation–ultrafiltration (UF) treatment of wildfire-affected soil leachate. The effects of coagulant type, dose, and pH on coagulation performance, membrane fouling, permeate quality, and fouling mechanisms were evaluated.

Without pre-coagulation, severe reversible and irreversible fouling occurred due to elevated turbidity, dissolved organic carbon (DOC), and aromatic organic matter. At neutral pH, chitosan outperformed ACH at a substantially lower optimal dose (3 mg/L versus 10 mg/L), achieving greater turbidity, DOC, and UV_{254} removal through combined charge neutralization and polymer bridging. Chitosan formed larger, more porous flocs, resulting in slower flux decline and reduced pore blocking and cake-layer formation. Although DOC and UV_{254} removal by chitosan was highest near pH 6, fouling mitigation was most effective at pH 7. At lower pH, excess protonated chitosan adsorbed onto the negatively charged membrane surface, increasing fouling resistance, as supported by SEM–EDS, contact angle, zeta potential, and ATR-FTIR analyses.

Chitosan pre-coagulation also improved UF permeate quality by enhancing removal of aromatic DOM, including humic- and fulvic-like fractions. Overall, this study demonstrates that chitosan is a promising alternative to aluminum-based coagulants for improving UF treatment of wildfire-affected soil leachate, although further validation with real post-fire source waters is needed.

1. Introduction

Forested watersheds are critical to global water security, supplying a significant portion of drinking water worldwide [1]. In the United States alone, approximately 60–65% of the nation's source water originates from these forested landscapes [2,3]. However, climate change and increased fuel loads in forests have increased the frequency of large, high severity wildfires, which can create substantial challenges for the protection and treatment of these critical water sources. Wildfire converts vegetation and surface organic matter into pyrogenic materials and alters soil physicochemical properties, thereby modifying runoff pathways, increasing erodibility, and enhancing the mobilization of sediments and solutes during subsequent precipitation events [4–10]. As a result, burned watersheds can export elevated loads of ash, particulate matter, dissolved organic matter (DOM), nutrients, and metals to downstream surface waters.

Post-wildfire water quality responses, however, are highly variable. Their magnitude, direction, and persistence depend strongly on watershed characteristics, hydrologic conditions, burn severity, and event timing. For example, turbidity has been reported to spike to as high as 800 FNU immediately following some wildfires in California, whereas post-wildfire turbidity in Oregon has generally not exceeded 300 NTU [11]. DOC responses are similarly variable. A recent review found that post-wildfire organic carbon increased in about 50% of studies across the western United States, whereas shifts in the western Pacific Northwest were often minimal and strongly influenced by storm events,

* Corresponding author.
E-mail address: xue.jin@oregonstate.edu (X. Jin).

https://doi.org/10.1016/j.seppur.2026.138996
Received 16 April 2026; Received in revised form 6 June 2026; Accepted 16 June 2026
Available online 17 June 2026

precipitation, vegetation, and hydrology [12]. Consistent with this pattern, Wampler et al. [13] reported that post-fire stream DOC concentrations can decrease by approximately 1.4–1.6 mg/L in high-severity burned areas under some seasonal conditions, while subsequent work showed that both DOC concentration and DOM composition are governed not only by burn severity, but also by hydrologic, meteorological, and landscape factors [14]. Specifically, DOM aromaticity and nitrogen content tend to increase with burn severity, although total DOC responses can range from minimal change to pronounced episodic pulses during storm events [14] [15]. Wildfire effects on metals and trace elements are likewise site dependent. Magliozzi et al. [16] reported substantial increases in trace metals such as Cr, Cu, Ni, Pb, and Zn after severe fire, with some concentrations exceeding U.S. EPA aquatic life acute criteria, whereas other burned watersheds have shown comparatively limited trace-element responses [17,18]. Collectively, these findings highlight the highly site-specific and event-driven nature of post-wildfire water quality degradation.

This variability is highly relevant to drinking water treatment. Many surface waters normally exhibit relatively low turbidity and DOM and can be treated effectively under routine operating conditions [12,19]. After wildfire, however, episodic increases in particulates, organic matter, metals, and other constituents can shift source waters beyond the design envelope of many existing treatment systems [12,19–21]. These changes can compromise treatment performance and intensify fouling and operational challenges, particularly for membrane-based systems that are highly sensitive to feed-water quality. Consequently, more robust and practical treatment strategies are needed to ensure reliable drinking water production under increasingly variable post-wildfire conditions [22].

Among advanced drinking water treatment processes, low-pressure membrane systems such as ultrafiltration (UF) have been increasingly adopted because of their compact footprint, high treatment efficiency, operational simplicity, and flexibility [23]. UF membranes, typically with pore sizes of 0.01–0.1 um and molecular weight cut-off values of 10–100 kDa, effectively remove suspended solids, bacteria, and larger organic fractions primarily through size exclusion [23–26]. However, wildfire-affected source waters often contain elevated concentrations of low-molecular-weight (<1 kDa), hydrophilic, and humic-like DOM [27–29]. Because these constituents are substantially smaller than the nominal pore diameters of UF membranes, they are poorly retained [30,31]. Instead, these smaller DOM fractions can penetrate membrane pores, adsorb within the internal pore structure, and/or contribute to the formation of dense, compact fouling layers on the membrane surface. These processes accelerate membrane fouling, resulting in rapid flux decline, increased hydraulic resistance, and deterioration of overall system performance [30]. Despite extensive research on UF membrane fouling, the extent to which the distinct chemical characteristics of wildfire-derived DOM influence fouling mechanisms and their subsequent controllability remains insufficiently understood.

Membrane fouling can be mitigated through various techniques, including membrane surface modification, synthesis of novel hydrophilic membrane materials [32,33], ozonation [34–36], quorum quenching (QQ) [37] and pre-coagulation [38,39]. Among these approaches, QQ is an important biological fouling-control strategy that reduces biofilm formation by disrupting microbial signaling. However, fouling during short-term UF treatment of wildfire-affected soil leachate is primarily driven by suspended particles, DOM, inorganic constituents, and their interactions with the membrane surface [38]. Therefore, this study focuses on physicochemical pre-coagulation as a practical strategy to reduce particulate, organic, and inorganic foulant loading prior to UF. Pre-coagulation is particularly relevant because of its cost-effectiveness, operational simplicity, and ability to aggregate fine particles and DOM into larger flocs, thereby altering the particle size distribution and reducing deleterious interactions between foulants and the membrane surface [23,39]. The efficiency of coagulation is highly dependent on the coagulant chemistry (organic vs. inorganic) and the specific dosage applied, particularly in the complex matrices of wildfire-impacted waters [38]. Inorganic coagulants, such as aluminum- and iron-based salts, are predominantly used in drinking water treatment plants due to their established efficacy and widespread availability [40]. These coagulants primarily function through charge neutralization and sweep flocculation, whereby destabilized colloidal and dissolved constituents are aggregated into larger, settleable flocs. By promoting the removal of these aggregates via sedimentation or straining prior to membrane filtration, inorganic pre-coagulation reduces particulate and organic loading on the membrane surface, thereby mitigating the rate of fouling development [41–43]. While effective, inorganic coagulants can generate large volumes of sludge containing residual metal species and may raise concerns regarding residual aluminum in treated water [44]. These limitations have motivated interest in alternative coagulants that can achieve comparable or improved performance with reduced chemical inputs and secondary impacts.

One such coagulant is chitosan, which has received growing attention in drinking water treatment. Chitosan is a natural and non-toxic cationic biopolymer produced through the deacetylation of chitin, a structural polysaccharide abundant in the exoskeletons of crustaceans such as shrimp and crabs [45]. Chitosan offers several advantages over traditional inorganic coagulants, including its dual functionality as both a coagulant and flocculant. Its long polymeric chains bearing positively charged amine groups enable efficient contaminant removal through a combination of charge neutralization and interparticle bridging [39]. In addition, chitosan is biodegradable, poses minimal health concerns, and generates sludge that can be beneficially reused as a soil amendment [46]. Recently, we demonstrated that integrating chitosan coagulation with UF is particularly effective for treating waters impacted by harmful algal blooms (HABs), which pose significant challenges to conventional membrane-based processes by intensifying membrane fouling and releasing cyanotoxins [39,47]. Our results showed that chitosan pre-coagulation can substantially improve treatment efficiency and mitigate membrane fouling by promoting the aggregation and removal of particulate and dissolved foulants prior to membrane filtration. In addition, chitosan coagulation–UF can enhance the removal of extracellular microcystin-LR, a prevalent and potent cyanotoxin, through toxin encapsulation within chitosan-induced flocs and subsequent membrane retention. These findings highlight the unique capacity of chitosan to simultaneously address fouling control and dissolved toxin removal in HAB-impacted waters.

Building on this prior evidence, we hypothesized that chitosan may also outperform conventional inorganic coagulants in the treatment of wildfire-affected waters, where enhanced coagulation is required for effective disinfection by-product (DBP) control [38,48–51]. Enhanced coagulation differs from conventional (simple) coagulation in that, whereas simple coagulation primarily targets turbidity removal, enhanced coagulation aims to maximize the removal of both turbidity and DOM [52]. This distinction is critical for limiting DBP formation, as DOM serves as a primary precursor for DBPs during disinfection processes [53]. Wildfire-impacted waters often contain elevated concentrations of DOM with stronger aromatic character and optical signatures associated with humic- and fulvic-type fractions, along with predominantly negative charge and high chemical reactivity [38,54]. Such constituents can be effectively removed via charge neutralization and interparticle bridging mechanisms, both of which chitosan can achieve efficiently, often at substantially lower doses than conventional aluminum-based coagulants [38]. However, as a high–molecular-weight biopolymer, chitosan may also contribute to membrane fouling, raising concerns regarding its overall performance in hybrid coagulation–UF systems. Accordingly, a systematic evaluation is needed to identify an optimal chitosan dose that maximizes turbidity and DOC removal while minimizing UF membrane fouling. To the best of our knowledge, no prior study has comprehensively evaluated chitosan as a standalone pre-coagulant for wildfire-affected waters while simultaneously optimizing enhanced coagulation performance and ultrafiltration fouling

mitigation under inline coagulation conditions.

In our study, we systematically evaluated chitosan as a potential alternative to the conventional inorganic coagulant aluminum chlorohydrate (ACH) in a hybrid coagulation–UF treatment process for a wildfire-affected soil leachate. The specific objectives were to: (1) quantify the effects of coagulant type and dosage on coagulation performance, including turbidity and DOC removal; (2) identify the optimal coagulant dosage that maximizes enhanced coagulation performance while mitigating UF membrane fouling through alterations in floc characteristics and dominant fouling pathways; and (3) assess the influence of solution pH on chitosan coagulation performance. The findings provide process-level mechanistic insight into coagulation–ultrafiltration performance using a controlled wildfire soil leachate analog, particularly illustrating how coagulant chemistry influences floc characteristics and membrane fouling behavior. These results help identify coagulant selection and operating conditions that enhance DOC removal and mitigate fouling within the defined experimental framework. Although this study provides process-level insight into coagulation–UF treatment of wildfire-affected soil leachate, it does not aim to comprehensively characterize temporal and spatial variability in real post-fire source waters. In watersheds, post-fire water quality is governed by burn severity, vegetation type, soil properties, watershed geochemistry, hydrologic connectivity, antecedent moisture, storm timing, and post-fire recovery. However, the system investigated here represents a simplified, laboratory-generated leachate and does not capture the hydrologic, geochemical, and compositional variability inherent to in-stream post-fire waters. Therefore, these findings should be interpreted as mechanistic proof-of-concept results within a clearly defined experimental scope. Additional validation using replicated soils across a broader range of burn severities, together with real-time in-stream post-fire samples, will be required before extending these conclusions to field-scale wildfire-impacted source waters.

2. Materials and methods

2.1. Site description, soil sampling, and leachate preparation

In this study, soil was collected from a single low-severity burned site within the 2023 Bedrock Fire perimeter on industrial forest land in the headwaters of Fall Creek, east of Springfield, Oregon, USA. The Bedrock Fire was ignited on July 22, 2023, and burned approximately 12,785 ha along the western slopes of the Cascade Mountains before containment in October 2023. Burn severity across the fire perimeter was classified using the differenced Normalized Burn Ratio (dNBR) derived from Monitoring Trends in Burn Severity (MTBS) data [55], with approximately 48% of the burned area classified as low severity, 25% as moderate severity, and 15% as high severity, while the remainder was unburned. The study area has a warm-summer Mediterranean climate, with cool, wet winters and warm, dry summers. Approximately 95% of annual precipitation occurs between October and June [56,57]. The 30-year mean annual precipitation is approximately 1700 mm and the mean annual air temperature is approximately 10 °C. Vegetation in the area is dominated by Douglas-fir (*Pseudotsuga menziesii*) across multiple age classes associated with timber harvest rotations. The sampled site was located at an elevation of approximately 550–600 m in terrain underlain by volcanic geology with well-drained, mesic, loamy soils [58].

Soil sampling was conducted in February 2024, approximately four months after fire containment. Although preliminary burn severity maps [59] and field observations were used during site reconnaissance, only one low-severity burned site was selected for subsequent laboratory testing in this study. At the selected site, surface soil (0–3 cm) was collected using a clean stainless-steel trowel or shovel by gently scraping the ground surface. The collected soil was used as the source material for preparing the wildfire-impacted leachate used in coagulation and ultrafiltration experiments. After collection, the soil was spread in thin layers on aluminum drying trays and air-dried at room temperature in the laboratory until mass stabilization (~10 days). Dried samples were then stored at 4 °C in the dark until leachate preparation.

Soil leachate was prepared following the method described previously [38], Briefly, 5 g of air-dried soil (see Supplementary Information, Fig. S1) that was added to 1 L of deionized (DI) water and mixed at 406 rpm for 24 h in the dark at room temperature. After mixing, suspensions were allowed to settle for 30 min to facilitate sedimentation of coarse particles. The supernatant was subsequently filtered through a 970 μm screen to remove remaining large particulates while retaining fine suspended material representative of post-fire runoff conditions. The leachate characteristics and representative images provided in Table 1 and Fig. S1 (Supplementary Information), respectively. Prior to coagulation, leachate pH was adjusted to 7.0 ± 0.1, 6.0 ± 0.1, or 5.0 ± 0.1 using 0.01 M HCl.

2.2. Materials

All chemicals used in this study were of either high-performance liquid chromatography grade or analytical grade. ACH, an inorganic coagulant commonly used in membrane-based drinking water treatment plants, was purchased from Spectrum Chemical (Gardena, CA). The ACH stock solution was prepared by dissolving 502 mg of ACH powder in 200 mL of DI water. Chitosan, (molecular weight: 150 kDa; degree of deacetylation: 95%; viscosity: 18 cP), used as an organic coagulant, was purchased from Primex (Siglufjordur, Iceland). The chitosan stock solution was prepared by dissolving 100 mg of chitosan in 10 mL of 1 M HCl, followed by sonication for 30 min at 60 °C. Next, 90 mL of DI water was added, and the solution was sonicated for an additional 30 min. The resulting mixture was then stirred at 300 rpm for 30 min to ensure complete dissolution. Stock solutions were freshly prepared prior to each experiment.

Flat-sheet polyvinylidene difluoride (PVDF) membranes with a nominal MWCO of 100 kDa were purchased from Synder Filtration (Vacaville, CA). Prior to use, circular coupons (effective surface area: 45 cm^2) were cut from a larger sheet and soaked in DI water for 24 h to fully wet the membrane and remove preservative chemicals. Membrane pore size was estimated from scanning electron microscopy (SEM) images of pristine membranes using ImageJ software by measuring 10 representative pores, yielding an average pore diameter of 21.6 ± 3.6 nm.

2.3. Experimental design

2.3.1. Coagulation

After leaching, coagulation was performed using a six-paddle programmable jar test apparatus (Phipps and Bird Inc., Richmond, VA) with ACH dosed at 0–30 mg/L and chitosan dosed at 0–5 mg/L. Following coagulant addition, the leachate was rapidly mixed at 300 rpm for 2 min to ensure complete and uniform dispersion, followed by slow mixing at 50 rpm for 30 min to promote floc formation. After

Table 1
Physicochemical characteristics of wildfire-affected soil leachate used in this study.

Parameter	Unit	Mean ± SD ($n = 3$)
pH	N/A	7.5 ± 0.1
Electrical conductivity	μS/cm	24.0 ± 0.3
Turbidity	NTU	1213 ± 33
DOC	mg/L	2.7 ± 0.1
UV_{254}	cm^{-1}	0.102 ± 0.005
$SUVA_{254}$	L/mg-m	3.7 ± 0.1
Alkalinity	mg/L as $CaCO_3$	6.00 ± 0.82
Major inorganic elements		
Al	mg/L	7.55 ± 0.05
Fe	mg/L	3.79 ± 0.04
Si	mg/L	13.20 ± 0.35

coagulation–flocculation, the suspension was passed through a 254 μm sieve to remove large flocs. This pre-treatment train is widely employed in membrane-based water treatment facilities. The sieved suspension was then transferred to the ultrafiltration feed tank for subsequent membrane filtration experiments.

2.3.2. Ultrafiltration experiments

Ultrafiltration experiments were conducted at a constant pressure of 40 psi (≈ 276 kPa) using compressed nitrogen in a dead-end stirred cell system (Millipore, Billerica, MA) with an effective membrane area of 45 cm^2. Permeate was collected in a beaker placed on a digital scale (OHAUS Navigator, NJ); the change in beaker weight was continuously recorded, and membrane flux was calculated from the weight change over time. Each filtration experiment consisted of four sequential steps: (1) membrane compaction, (2) fouling, (3) backwashing, and (4) post-cleaning DI water filtration. First, membranes were compacted by filtering DI water at 40 psi until a stable flux was achieved. Next, the precoagulated suspension was added to the stirred cell and filtered until 400 mL of permeate was collected. After suspension filtration, the cell was emptied, the membrane was physically flipped, the cell was refilled with DI water, and 400 mL of permeate was collected to perform backwashing. Finally, to evaluate fouling reversibility, the membrane was flipped back to its original filtration orientation and DI water was filtered again until 400 mL of permeate was collected.

The resistance-in-series model was used to quantify the distribution of membrane fouling resistance as shown below:

$$R_m = \frac{\Delta P}{\mu J_0} \tag{1}$$

$$R_{ir} = \frac{\Delta P}{\mu J_{DI}} - R_m \tag{2}$$

$$R_r = \frac{\Delta P}{\mu J_t} - R_m - R_{ir} \tag{3}$$

where ΔP is the transmembrane pressure, μ is the dynamic viscosity of the feed water; R_m, R_{ir}, R_r are the resistance of intrinsic membrane resistance, hydraulic irreversible fouling resistance, and hydraulic reversible fouling resistance, respectively; J_0, J_{DI}, J_t are the permeate flux of the pristine membrane, membrane after backwash, and membrane at the end of fouling test, respectively.

To identify the membrane fouling mechanism, the combined standard pore-blocking and cake filtration model was applied. Briefly, this model accounts for flux decline caused by both pore blockage and cake layer formation. Standard pore blocking occurs when smaller particles enter the membrane pores and block them, whereas cake layer formation becomes dominant once pores are partially or fully blocked and particles accumulate on the membrane surface [38,60]. The governing equations are given as follows:

$$V = \frac{2}{k_s}\left(\beta\cos\left(\frac{2\pi}{3} - \frac{1}{3}arc\ cos(\alpha)\right) + \frac{1}{3}\right) \tag{4}$$

$$\alpha = \frac{8}{27\beta^3} + \frac{4k_s}{3\beta^3 k_c J_0} + \frac{4k_s^2 t}{3\beta^3 k_c} \tag{5}$$

$$\beta = \sqrt{\frac{4}{9} + \frac{4k_s}{3k_c J_0} - \frac{2k_s^2 t}{3k_c}} \tag{6}$$

where, V is accumulative permeate volume, K_s is the standard pore-blocking constant, K_c is the cake filtration constant, and t is the filtration time. Model fitting was performed using nonlinear least squares regression implemented in MATLAB R2023b (MathWorks, Natick, MA). Model accuracy was evaluated using the root mean squared error (RMSE), standard error of the estimate (SEE), sum of squared errors (SSE) and coefficient of determination (R^2) with $R^2 \geq 0.95$ considered indicative of satisfactory model performance. Model uncertainty at the optimum coagulation doses was further evaluated using 95% confidence intervals for the fitted time–permeate-volume curves.

2.4. Water quality analysis

Water quality analyses were performed on leachate produced from a single burned-soil sample, as well as the screened suspension after straining, and the ultrafiltration permeate. Turbidity was quantified using a portable turbidity meter (2100Q, Hach Company, CO). Zeta potential was determined using a Zetasizer Nano series (Malvern Instruments, UK). The progression of floc growth was monitored using a photometric dispersion analyzer (PDA 3000, Rank Brothers Ltd., UK). Floc morphology was examined using a compound microscope (DM 2500, Leica Microsystems, Wetzlar, Germany). During the final 10 s of the flocculation step, flocs were gently collected from the center of the beaker using a 5 mL pipette with a widened, cut tip to minimize shear-induced disruption and prevent floc breakup. The collected flocs were immediately imaged. Floc size was calculated as the geometric mean diameter using the following equation:

$$d = (L \times W)^{0.5} \tag{7}$$

where L and W represent the measured length and width of an individual floc, respectively [61].

Dissolved organic carbon (DOC) was quantified using a Shimadzu TOC-L analyzer (Shimadzu Corp., Japan) following filtration of water samples through a 0.45 μm polyethersulfone membrane. UV absorbance at 254 nm (UV_{254}) was quantified using a 1-cm quartz cuvette on a UV–vis spectrophotometer (Orion AquaMate 8000, Thermo Scientific, WA). Specific UV absorbance ($SUVA_{254}$) was calculated as the ratio of UV_{254} to DOC. Alkalinity was measured using a Multiparameter Photometer for Water & Wastewater analysis (HI83300, Hanna Instruments Inc., RI). DOM composition was further characterized using excitation–emission matrix (EEM) fluorescence spectroscopy with a Cary Eclipse Fluorescence Spectrophotometer (Varian, Inc., CA), recording emission wavelengths from 300 to 600 nm at 1 nm intervals and excitation wavelengths from 200 to 400 nm at 5 nm intervals. Concentrations of aluminum (Al), iron (Fe), and silicon (Si) were measured using inductively coupled plasma mass spectrometry (iCAP RQ ICP-MS, Thermo Fisher Scientific, MA). These elements were quantified because they contribute to membrane fouling through inorganic deposition and metal–DOM complexation, which can enhance irreversible fouling [38].

2.5. Membrane characterization

Comprehensive analysis of both pristine and fouled membranes was performed using multiple complementary techniques. Membrane surface hydrophobicity was assessed using the sessile drop method with a contact angle goniometer (Ossila, England, UK). Zeta potential was measured through streaming potential assessments using the adjustable gap cell in a SurPASS electrokinetic analyzer (Anton Paar, Austria), with tests conducted in 10 mM KCl across a pH range of 3–8. The top-surface morphology of the membranes was investigated using an FEI Quanta 3D Field Emission Dual Beam Scanning Electron Microscope (SEM/FIB) equipped with a Horiba energy-dispersive X-ray spectroscopy (EDS) detector (7200-H, Kyoto, Japan) for elemental composition analysis. Before SEM–EDS analysis, membrane samples were cut into small pieces, affixed to specimen holders with double-sided carbon tape, and sputter-coated with Au/Pd to enhance surface conductivity. Surface functional groups were examined using Fourier-transform infrared spectroscopy (FTIR; Nicolet 6700, Thermo Fisher Scientific, MA) with a 42° single-reflection germanium attenuated total reflectance (ATR) element (Seagull™ variable angle reflection accessory).

2.6. Statistical analysis

Statistical analysis was performed using a paired *t*-test to evaluate the differences between ACH and chitosan in terms of turbidity removal, DOC removal, UV_{254} reduction, flux decline, and membrane resistance analysis. Statistical significance was evaluated at $p \leq 0.05$, while $0.05 < p \leq 0.10$ was interpreted as marginally significant. All statistical analyses were conducted using OriginPro 2026, Northampton, MA.

3. Results and discussion

3.1. Effect of coagulant type and dose on coagulation performance

Across three experimental runs, chitosan outperformed ACH in removing turbidity and DOM, achieving higher removal efficiencies at lower dosages (Fig. 1). At the optimal dose of 3 mg/L, chitosan reduced turbidity by approximately 53–56%, which was significantly higher than ACH at its optimal dose of 10 mg/L (paired *t*-test, $p = 0.003$). Chitosan also achieved ~40% DOC removal, significantly exceeding the ~30% DOC removal achieved by ACH under its optimal condition (paired t-test, $p = 0.031$).

The untreated leachate was characterized by high turbidity (~1200 NTU), moderate DOC (~2.8 mg/L), and pronounced aromatic character. This turbidity should be interpreted as an extreme post-fire sediment-mobilization scenario rather than typical routine source-water quality. Under actual utility operation, water of this turbidity would likely trigger operational responses such as source switching, bypass, blending, sedimentation, clarification, or enhanced pretreatment. However, turbidity values on the order of 10^3 NTU have been documented during intense post-wildfire storm events [62–64], particularly during first-flush mobilization of ash and sediment. Therefore, this high-solids leachate was used as a controlled stress-test matrix to compare coagulant-specific floc formation and UF fouling behavior under severe but environmentally plausible conditions. Optical characterization further indicated dominance of aromatic DOM fractions. EEM spectra (Fig. S3a) showed strong humic- and fulvic-like fluorescence regions relative to protein-like and microbial by-product regions. In parallel, a $SUVA_{254}$ value of ~3.73 L /mg C/m suggested moderate aromaticity [15,38] [65,66]. Together, these observations confirm that the leachate represented a high-solids matrix containing appreciable aromatic DOM fractions for evaluating coagulation–UF performance.

ACH coagulation resulted in only modest improvements in turbidity and DOC removal compared with the untreated leachate. Turbidity decreased from ~1200 NTU to 970 NTU at 10 mg/L ACH, corresponding to ~20% removal (Fig. 1a). The limited reduction suggests the formation of relatively small aluminum hydroxide flocs, as indicated by our PDA results (Supplementary Information, Fig. S4a), which were capable of passing through the 254 μm screening step. Increasing ACH dosage beyond 10 mg/L led to increased residual turbidity, consistent with overdosing effects such as charge reversal, formation of fine aluminum hydroxide precipitates, and particle re-stabilization [38,39]. DOC removal followed a similar pattern, reaching a maximum of ~30% at 10 mg/L before slightly declining at higher doses, indicating possible saturation of adsorption sites on aluminum hydroxide flocs [38].

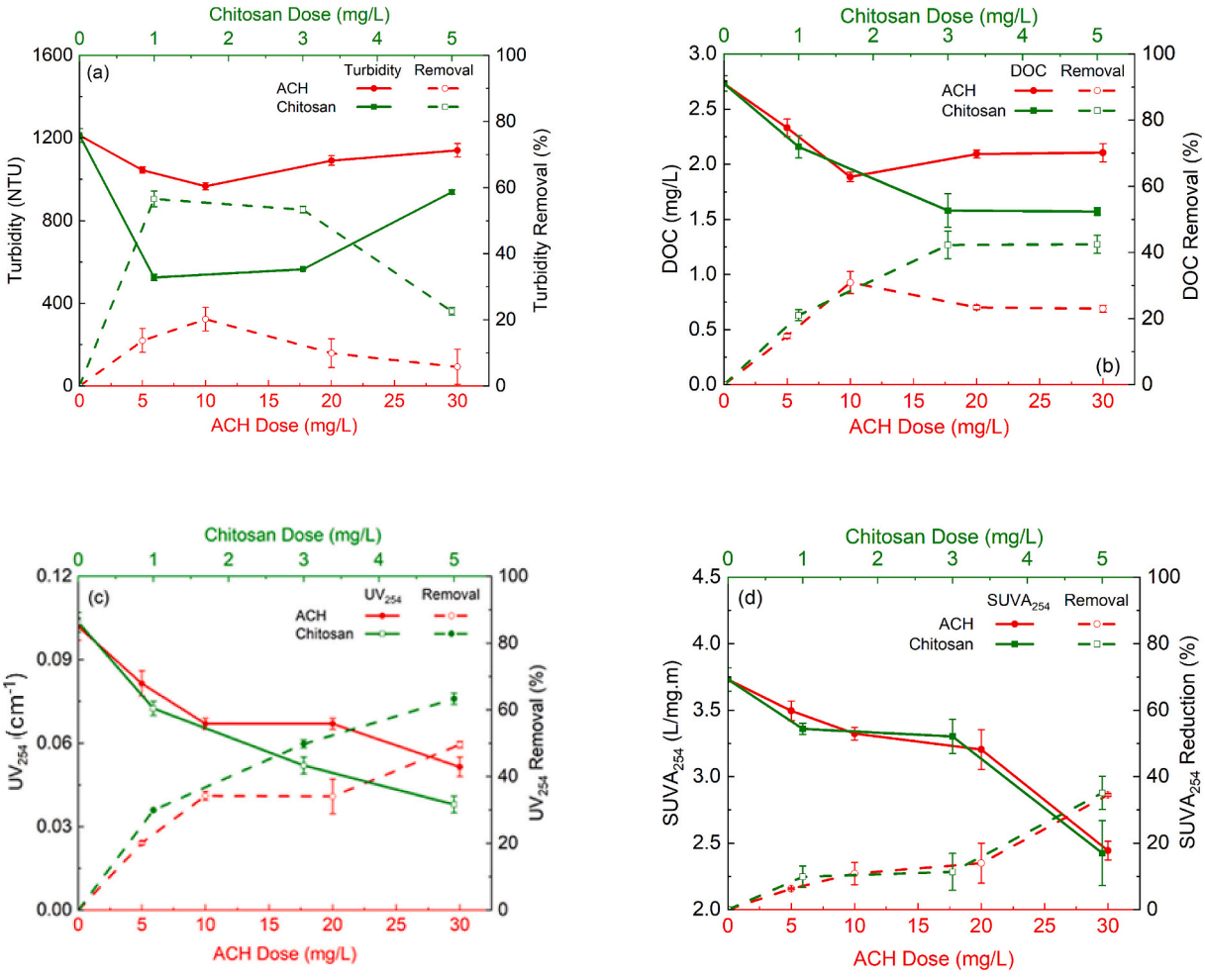

Fig. 1. Effect of coagulant type and dosage on coagulation performance: (a) turbidity removal, (b) DOC removal, (c) UV_{254} removal and (d) $SUVA_{254}$ reduction.

In contrast, chitosan demonstrated greater efficiency at lower dosages. Between 1 and 3 mg/L, turbidity decreased to ~500 NTU (~53–56% removal), indicating the formation of larger and more readily sievable flocs [39]. Further increasing the chitosan dosage to 5 mg/L led to a marked decline in turbidity removal, suggesting overdosing effects such as charge reversal and particle re-stabilization. DOC removal reached ~40% at 3 mg/L, reducing DOC to approximately 1.5 mg/L. Additional increases in chitosan dosage did not further improve DOC removal, indicating saturation of active binding sites along the chitosan polymer chains [67]. Accordingly, 3 mg/L was identified as the optimal chitosan dose. Although 3 mg/L chitosan substantially improved leachate quality, the residual turbidity remained higher than typical UF feed-water conditions in conventional drinking-water operation. Therefore, this leachate should be interpreted as a challenging high-solids matrix rather than a conventional plant influent. The coagulation–UF experiments were designed to simulate an inline coagulation–membrane filtration configuration, in which coagulation/flocculation was followed directly by UF without a dedicated sedimentation step, allowing direct evaluation of coagulant–floc–membrane interactions. Under practical treatment conditions, additional solids-separation steps such as sedimentation may further improve feed-water quality before UF, as supported by the supplemental 5-min sedimentation experiment (Fig. S4, Supplementary Information).

UV_{254} removal trends further illustrate mechanistic differences. With ACH, UV_{254} and $SUVA_{254}$ decreased gradually with increasing dose, indicating preferential removal of aromatic, hydrophobic DOM fractions even when bulk DOC removal plateaued. However, UV_{254} removal by ACH remained lower than that achieved by chitosan. At the optimal dose, chitosan achieved ~50–60% UV_{254} removal, which was significantly higher than that achieved by ACH under its optimal condition (paired *t*-test, $p = 0.008$). The comparable reduction in $SUVA_{254}$ suggests that both coagulants preferentially removed aromatic, hydrophobic, and higher-molecular-weight DOM fractions, such as humic- and fulvic-like substances, while leaving behind more hydrophilic, low-molecular-weight, and less aromatic DOM fractions that are less amenable to coagulation. These compositional differences are important for coagulant dosing because readily destabilized aromatic and hydrophobic fractions can be removed at lower doses, whereas more hydrophilic and low-molecular-weight DOM may require higher doses or remain poorly removed even after dose optimization. The greater DOC and UV_{254} removal by chitosan indicates that chitosan removed a broader fraction of total DOM than ACH, likely due to combined charge neutralization and polymer-bridging interactions.

Collectively, in our study chitosan's combined charge neutralization and polymer-bridging mechanisms [68] more effectively destabilized wildfire-derived particulates and aromatic DOM under extreme turbidity conditions. Enhanced upstream removal of these fractions is expected to mitigate subsequent ultrafiltration membrane fouling and reduce disinfection by-product (DBP) precursor loading, given the strong relationship between DOC, UV_{254}, and DBP formation [69–71]. Both ACH and chitosan exhibited clear overdosing thresholds beyond which removal efficiency declined, highlighting the importance of dose optimization, particularly under high-solids, extreme-event water quality scenarios.

3.2. *Effect of coagulant type and dose on UF membrane fouling*

Chitosan pre-coagulation markedly reduced UF membrane fouling

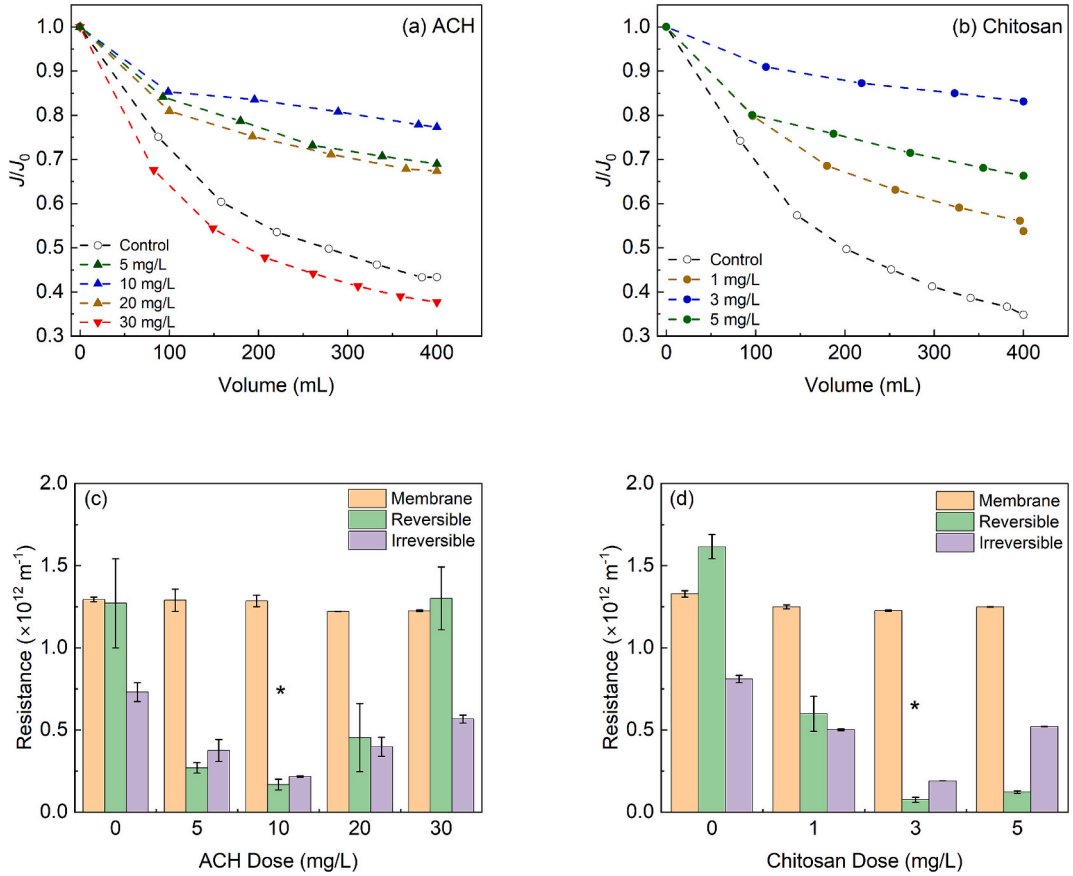

Fig. 2. Effect of ACH and chitosan pre-coagulation on ultrafiltration membrane flux decline and fouling resistance: (a) and (b) show the normalized permeate flux (J/J_0) as a function of filtered volume for ACH and chitosan pre-coagulation, respectively. (c) and (d) present fouling resistances at different coagulant dosages. * indicates optimal dose.

compared to both ACH and the no-coagulation control, achieving substantially lower flux decline and fouling resistances at a lower optimal dose (Fig. 2). At 3 mg/L chitosan, flux decline was limited to ~10%, whereas the optimal ACH dose (10 mg/L) resulted in ~18% flux decline (paired *t*-test, $p = 0.059$). In contrast, the absence of pre-coagulation led to severe fouling, with ~55% flux loss after filtration of 400 mL of burned soil leachate.

In the absence of pre-coagulation (control), flux declined rapidly during the early stages of filtration, indicating severe initial pore constriction followed by progressive surface cake formation [72]. Resistance-in-series analysis confirmed that both reversible (1.25×10^{12} m^{-1}) and irreversible (0.75×10^{12} m^{-1}) fouling resistances were high under control conditions (Fig. 2c). The rapid early decline suggested that fine particulates and dissolved organic fractions were able to access and obstruct membrane pores. As filtration proceeded, accumulated solids contributed to cake layer formation, further increasing hydraulic resistance.

Pre-coagulation substantially mitigated fouling. With ACH, flux reduction was dose-dependent. At 5 mg/L, flux decline decreased to ~25%, and at 10 mg/L it further decreased to ~18%, corresponding to the maximum turbidity and DOC removal observed in Section 3.1. At this optimal ACH dose, reversible and irreversible fouling resistances decreased to 0.14×10^{12} m^{-1} and 0.25×10^{12} m^{-1}, respectively. The standard blocking constant ($Ks = 0.26$ m^{-1}) and cake layer constant ($Kc = 2798.40$ s/m^2) were minimized, indicating reduced pore obstruction and slower cake buildup. However, increasing ACH dosage beyond 10 mg/L increased fouling resistances and model constants, consistent with overdosing effects such as colloidal re-stabilization and formation of fine aluminum hydroxide–organic complexes [73], some of which penetrated membrane pores while others accumulated on the membrane surface, thereby exacerbating fouling.

Chitosan exhibited superior fouling mitigation at substantially lower doses. At 1 mg/L, flux decline was reduced by nearly half relative to the control. At the optimal dose of 3 mg/L, flux decline was limited to ~10%, which was marginally lower than that observed under the optimal ACH condition (paired *t*-test, $p = 0.059$). Reversible fouling resistance decreased to 0.06×10^{12} m^{-1}, which was significantly lower than that under the optimal ACH condition (paired t-test, $p = 0.012$), while irreversible fouling resistance decreased to 0.20×10^{12} m^{-1} (Fig. 2d). The corresponding blocking ($K_s = 0.15$ m^{-1}) and cake formation ($K_c = 1559.40$ s/m^2) constants were approximately half those observed at the optimal ACH dose, indicating substantially reduced pore constriction and slower cake layer development. The improved performance of chitosan is consistent with its enhanced removal of turbidity and optically characterized aromatic DOM fractions (Section 3.1). Through charge neutralization and polymer-bridging mechanisms, chitosan likely formed larger and more porous flocs that acted as a dynamic pre-filter, defined here as a permeable floc layer that reduced the transport of fine particulates and dissolved organic components to the membrane surface, thereby limiting pore constriction and slowing cake-layer development. However, increasing the chitosan dose beyond the optimum to 5 mg/L caused a greater flux decline of approximately 30% and increased irreversible resistance. This deterioration suggests a chitosan overdosing effect, likely caused by excess polymer remaining in solution, accumulating on the membrane surface, or penetrating into membrane pores, thereby increasing hydraulic resistance [39]. In contrast, ACH removal was more limited and more sensitive to overdosing effects.

Overall, our findings demonstrated that severe fouling under control conditions resulted from the combined influence of extreme suspended solids loading and aromatic DOM, which could occur during runoff events from wildfire-impacted areas. In our study, pre-coagulation mitigated both pore obstruction and cake layer formation, with minimum fouling observed at optimal dosages. Notably, chitosan achieved lower flux decline and reduced reversible fouling at a substantially lower dose than ACH, underscoring its potential effectiveness under high-solids, extreme-event conditions. Further insight into irreversible fouling mechanisms is provided through membrane characterization analyses presented in Section 3.4.

3.3. Effect of pH on chitosan coagulation and fouling behavior

The coagulation performance of chitosan is strongly dependent on solution pH due to the protonation–deprotonation of amine groups along the chitosan polymer chain [74]. Therefore, the effect of pH on chitosan coagulation performance and membrane fouling control was further evaluated at its optimal dose of 3 mg/L. As shown in Fig. 3, turbidity removal was relatively insensitive to pH, remaining nearly constant at 55–56% across pH 5–7. This behavior suggests that suspended particle destabilization was effectively achieved over the tested pH range and was not strongly governed by chitosan speciation under the applied conditions.

In contrast, DOC and UV_{254} removal exhibited a clear pH dependence. Both parameters reached their highest removal efficiencies at pH 6, with DOC and UV_{254} removals of 49% and 68%, respectively. These removals were significantly higher than those at pH 5 (paired *t*-test, $p = 0.035$ for DOC and $p = 0.049$ for UV_{254}) and pH 7 (paired t-test, $p = 0.035$ for DOC and $p = 0.016$ for UV_{254}). This trend reflects the pH-dependent balance between chitosan charge density and polymer chain conformation. Near its pK_a (6.2–6.5) [75], chitosan is partially protonated, providing sufficient positive charge to electrostatically interact with negatively charged DOM while maintaining a moderately extended polymer conformation. This configuration facilitates simultaneous charge neutralization and limited polymer bridging, which is particularly effective for the removal of aromatic, UV-absorbing DOM. At pH 5, chitosan is more extensively protonated, resulting in a high charge density. While this enhances charge neutralization, strong intramolecular electrostatic repulsion among closely spaced $–NH_3^+$ groups constrains polymer chain extension in solution. Consequently, long-range interparticle bridging is suppressed, favoring the formation of relatively small, compact aggregates [76], as reflected by the reduced floc size (relative to pH 7) observed in the PDA measurements (Supplementary Information, Fig. S5a). This diminished polymer bridging also limits effective DOM aggregation. Conversely, at pH 7, decreased protonation weakens electrostatic interactions between chitosan and DOM, diminishing DOC and UV_{254} removal despite the increased contribution of polymer bridging. Collectively, these results indicate that pH 6 provides the most favorable balance between electrostatic attraction and polymer bridging for enhanced removal of DOM by

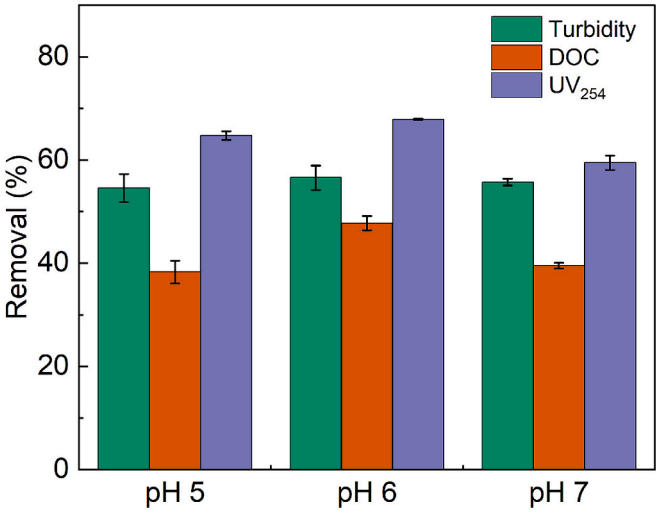

Fig. 3. Effect of pH on turbidity, DOC, and UV_{254} removal by chitosan coagulation (3 mg/L) followed by straining.

chitosan.

Floc morphology (Fig. S6, Supplementary Information) and size analysis (Fig. S7, Supplementary Information) further supported the pH-dependent behavior of chitosan coagulation. The control sample contained fine, dispersed particles with minimal aggregation and an average particle size of approximately 17 μm. ACH at its optimum dose formed relatively small flocs with an average size of approximately 86 μm, consistent with compact aggregates produced mainly through charge neutralization and sweep flocculation. In contrast, chitosan at pH 7 produced substantially larger and more interconnected flocs with an average size of approximately 201 μm, reflecting the combined effects of charge neutralization and polymer bridging. These larger and more open flocs were more effective at limiting pore-scale fouling, consistent with the improved flux behavior and fouling-model results (Fig. 4, Table 3). At pH 5 and 6, chitosan flocs became less interconnected and more fragmented, suggesting weakened bridging interactions under acidic conditions. Because ionic strength, detailed DOM speciation, and direct floc zeta potential were not independently quantified in this study, the proposed pH-dependent mechanism should be interpreted as an integrated explanation based on bulk zeta potential, floc morphology, floc size, DOC/UV_{254} removal, and membrane fouling behavior.

Despite improved coagulation performance at pH 6, chitosan demonstrated the best fouling control efficiency at pH 7 where the minimum flux decline occurred (Fig. 4). When pH decreased from 7 to 6 and further to 5, flux decline became progressively more severe. At pH 7, flux remained above 83% of the initial value at the end of filtration, significantly higher than that at pH 6 (64%; paired *t*-test, $p = 0.007$) and pH 5 (50%; paired t-test, $p = 0.001$). This deterioration in fouling control with decreasing pH indicates that improved coagulation performance does not directly translate to enhanced membrane protection. Instead, fouling behavior is governed by the characteristics of the formed flocs and residual dissolved species. At lower pH, reduced DOM negativity [77,78] combined with highly protonated chitosan leads to an effective excess of positively charged polymer in solution (Fig. S5b, Supplementary Information). This excess chitosan can readily adsorb onto the negatively charged PVDF membrane surface, accelerating fouling even when bulk-phase DOM removal is enhanced.

These trends are further supported by the resistance-in-series analysis (Fig. 4b) and the combined standard pore-blocking and cake filtration model (Table 3). Both reversible and irreversible fouling resistances increased markedly as pH decreased from 7 to 6 and 5. The elevated fouling resistance at lower pH can be attributed to two synergistic mechanisms. First, flocs formed at pH 5 and pH 6 were smaller and denser, as indicated by PDA measurements (Supplementary Information, Fig. S4a), providing less effective shielding against pore-scale fouling. Such compact aggregates are more prone to penetrate membrane pores or form dense, hydraulically resistant cake layers. Second, excess protonated chitosan at lower pH strengthens electrostatic attraction to the negatively charged membrane surface, thereby promoting adsorption-driven irreversible fouling. Overall, these results indicate that although pH 6 favors DOC and UV_{254} removal (Fig. 3), neutral pH provides the best overall performance for inline coagulation–ultrafiltration by minimizing membrane fouling. Given that surface water pH typically falls within the range of 6.5–7.5, pH adjustment is not required when chitosan is applied as a coagulant in inline coagulation–ultrafiltration systems.

3.4. Fouled membrane characterization and fouling mitigation mechanisms

Based on the results in Sections 3.1–3.3, chitosan achieved superior fouling control at a much lower optimal dose than ACH, reducing both reversible and irreversible fouling. This improvement can be partly attributed to chitosan's enhanced removal of turbidity, DOC, and aromatic organic matter (UV_{254}), which substantially decreased foulant loading to the membrane module. In addition, it was found that chitosan exhibited the highest fouling mitigation efficiency at neutral pH, with diminished performance at pH 5 and 6. To further elucidate the mechanisms governing fouling mitigation, particularly the most problematic irreversible fouling, the membrane surface morphology, elemental composition, wettability, surface charge, and functional group chemistry were systematically characterized after filtration and backwash under different coagulation conditions using SEM (Fig. 5), EDS (Table 4), contact angle measurements (Fig. 6a), zeta potential (Fig. 6b) analysis, and ATR-FTIR spectroscopy (Fig. 6c).

Collectively, these complementary techniques establish a clear baseline for the pristine PVDF membrane. SEM imaging revealed a homogeneous surface with well-defined pore structures. Elemental analysis showed that the surface was dominated by carbon and fluorine, consistent with the PVDF polymer matrix. The pristine membrane exhibited a high water contact angle of 74°, confirming its inherently hydrophobic nature [79]. FTIR spectra displayed characteristic PVDF absorption bands at ~1400 cm^{-1} (–CH_2– stretching) and at 1275, 1165, 877, and 837 cm^{-1} (–CF_2– vibrations). Zeta potential measurements further indicated that the pristine membrane maintained a negative surface charge across the entire pH range tested.

Following filtration of the burned soil leachate without pre-coagulation (control), the membrane surface became heavily covered by a compact and heterogeneous fouling layer. The water contact angle decreased to 34°, and the zeta potential became more negative, indicating that hydrophilic and negatively charged particles and DOM remained strongly attached to the membrane surface even after backwash. A similar decrease in contact angle after burned soil leachate filtration was also reported by Farooq et al. [38]. SEM–EDS analysis revealed elevated oxygen, silicon, and aluminum contents, reflecting the

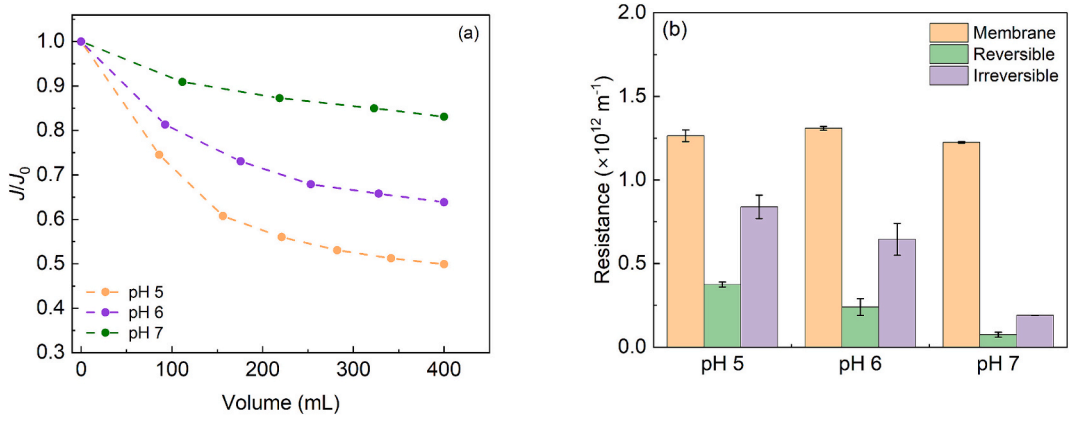

Fig. 4. Effect of pH on chitosan (3 mg/L) pre-coagulation performance: (a) normalized membrane flux (J/J_0) and (b) fouling resistance components.

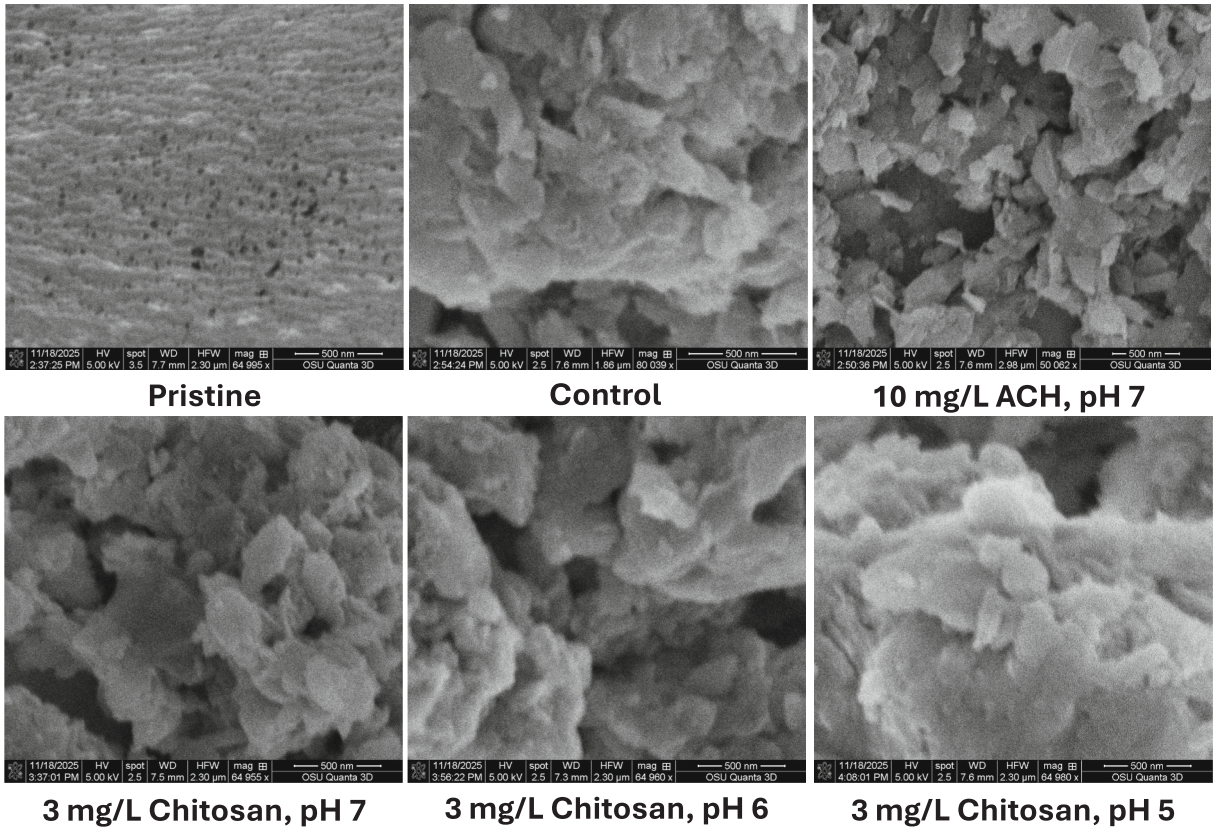

Fig. 5. SEM images of the pristine and fouled membranes after backwash.

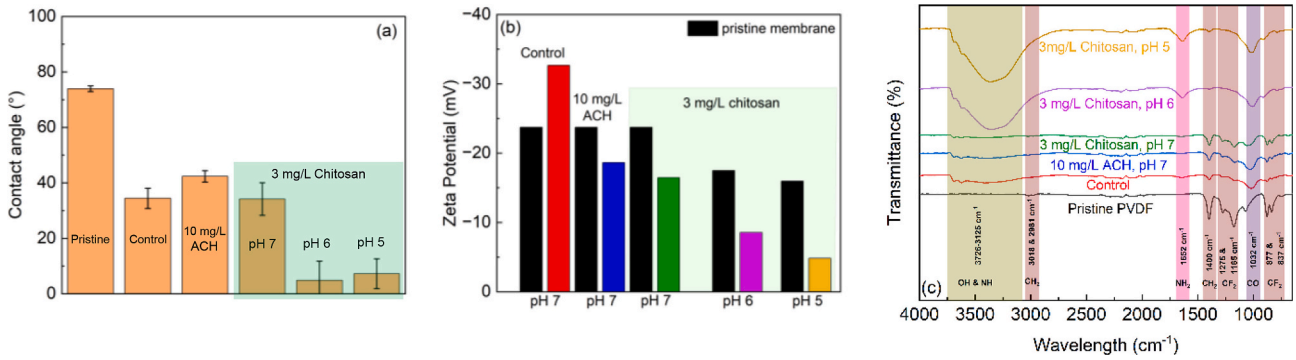

Fig. 6. Surface characterization of pristine and fouled membranes after backwash: (a) contact angel, (b) surface zeta potential, and (c) ATR-FTIR spectra.

deposition of mineral particulates and metal-associated DOM derived from a wildfire-impacted leachate. Concomitantly, the intensities of the intrinsic –CH_2– and –CF_2– bands decreased, consistent with surface coverage by foulants. Several new absorption features emerged, including broad –OH/–NH stretching bands (3100–3700 cm^{-1}), amide-related bands (~1650 cm^{-1}), and carbonyl (C=O) vibrations (~1032 cm^{-1}), confirming the accumulation of hydrophilic organic matter [80,81]. These functional groups facilitate complexation with multivalent metals such as Al [82], promoting the formation of strongly bound, chemically stable foulant layers that underpin irreversible fouling.

Pre-coagulation with ACH at the optimal dose (10 mg/L) reduced particulate and DOM loading to the membrane, it also markedly altered the fouling morphology, producing a more granular surface characterized by discrete aggregates distributed across the membrane. The aluminum content on the membrane surface increased to 16.6%, compared to 10.9% in the control. The fouled membrane remained hydrophilic, with a contact angle of 42°, indicating persistent coverage by hydrophilic materials. Together, these observations point to the accumulation of aluminum hydroxide precipitates and Al–DOM complexes on the membrane surface, which form compact, strongly bound deposits and contribute to irreversible fouling.

In contrast, chitosan pre-coagulation at its optimal dose (3 mg/L) and neutral pH produced a markedly different fouling morphology (Fig. 5). The membrane surface was covered by larger, more loosely packed, and porous aggregates, forming an open and heterogeneous layer. This structure is consistent with the formation of polymer-bridged flocs that act as a dynamic pre-filter, limiting direct contact between fine particulates and dissolved organics with the membrane surface and thereby mitigating pore-scale fouling [47]. The fouled membrane remained hydrophilic, with a contact angle of 34° (Fig. 6a). The membrane surface charge (−16.5 mV) was clearly reduced relative to both the pristine membrane (−23.7 mV) and the control (−32.7 mV), indicating effective charge neutralization among positively charged chitosan, negatively charged foulants, and the PVDF surface. Consistently,

the ATR-FTIR spectra exhibit a markedly attenuated –OH/–NH stretching band (3100–3700 cm^{-1}), confirming a thinner fouling layer on the membrane. Together, these results demonstrate that chitosan pre-coagulation at neutral pH fundamentally alters foulant structure and interfacial interactions, yielding a more permeable deposit layer.

When the pH decreased to 5 and 6, the FTIR spectra showed a substantial intensification of O–H/N–H stretching bands (3200–3600 cm^{-1}) and more pronounced absorption near 1650 cm^{-1}, indicating increased adsorption of protonated chitosan onto the membrane surface. The enhanced presence of amine-related functional groups confirms excessive polymer deposition under acidic conditions, consistent with the elevated oxygen and nitrogen contents (Table 4), the less negative surface zeta potential resulting from adsorption of positively charged chitosan, and the marked reduction in contact angle to below 7° (Fig. 6a). Although such adsorption renders the membrane surface highly hydrophilic, it simultaneously promotes the formation of a dense, hydrated fouling layer (Fig. 5), which increases hydraulic resistance. Together, these complementary characterization results provide molecular-level evidence that excessive chitosan deposition at acidic pH underlies the observed deterioration in fouling control, despite the slightly enhanced DOC and UV_{254} removal at pH 6 (Fig. 3).

Based on the above discussion, coagulant-specific fouling mitigation mechanisms can be proposed, as schematically illustrated in Fig. 7. In the absence of pre-coagulation, the leachate exhibited high turbidity, DOC, and UV_{254}, resulting in severe reversible and irreversible fouling. The relatively high $SUVA_{254}$ value (~3.8 L mg^{-1}/m) suggests the coexistence of hydrophobic and hydrophilic DOM fractions [83], which promote multiple fouling pathways, including hydrophobic interactions between aromatic DOM and the hydrophobic PVDF membrane [84], internal pore blockage by low-molecular-weight organics [85], and metal–DOM complexation [38,86,87]. As a result, pore blockage and cake layer formation occurred simultaneously, leading to rapid flux decline.

Pre-coagulation mitigated fouling, but its effectiveness depended strongly on coagulant type. For ACH, optimal performance was achieved at 10 mg/L, reducing turbidity, DOC, and UV_{254} by approximately 20%, 30%, and 34%, respectively, thereby lowering solids loading to the membrane. However, removal by ACH was governed primarily by charge neutralization and sweep flocculation, producing small and compact flocs, as confirmed by PDA analysis (Supplementary Information, Fig. S4a). During ultrafiltration, these dense aggregates promoted early-stage pore blockage and compact cake layer formation, resulting in approximately 20% flux decline. The corresponding pore-blocking and cake filtration constants (K_s = 0.26 m^{-1}; K_c = 46.6 min/m^2) indicate persistent internal fouling and the formation of a hydraulically resistant cake layer. When interpreted together with SEM observations of compact surface deposits and EDX evidence of aluminum-rich foulants, these results suggest that the small, dense flocs formed during ACH pre-coagulation can block membrane pores during the early stages of filtration, restricting water passage and leading to flux decline. The dominant fouling behavior in the ACH system is therefore attributed to compact floc deposition and persistent irreversible fouling associated with metal–DOM complexation, with hydrophobic interactions playing a secondary role.

In contrast, chitosan exhibited superior fouling mitigation at the optimal dose of 3 mg/L, achieving substantially higher turbidity (~53%), DOC (~42%), and UV_{254} (~50%) removal. At pH 7, partially protonated chitosan removed particles and DOM through a combined charge neutralization and polymer bridging mechanism, forming larger and more porous flocs. These flocs acted as a dynamic pre-filter, limiting pore-scale fouling and facilitating water transport through the cake layer [47]. Consequently, flux decline was reduced to approximately 10%, and both pore-blocking and cake filtration constants were nearly half of those observed for ACH (Table 2). Although some irreversible fouling persisted, chitosan clearly provided more effective fouling mitigation than ACH. The EDS results provide further evidence that inorganic and organic–inorganic foulants contributed to the remaining irreversible fouling. The detection of Al and Fe on the fouled membrane surface suggests that residual metal species, including metal hydroxides/oxides and possible metal–DOM associations, were retained after backwashing. These metal-associated foulants can enhance irreversible fouling because DOM functional groups, including carboxyl, phenolic, and hydroxyl groups identified by FTIR, can coordinate with multivalent metal ions to form stable organic–metal complexes [82,88,89]. Such complexes may adhere strongly to the membrane surface and resist removal by hydraulic backwashing. The $SUVA_{254}$ value of the chitosan-

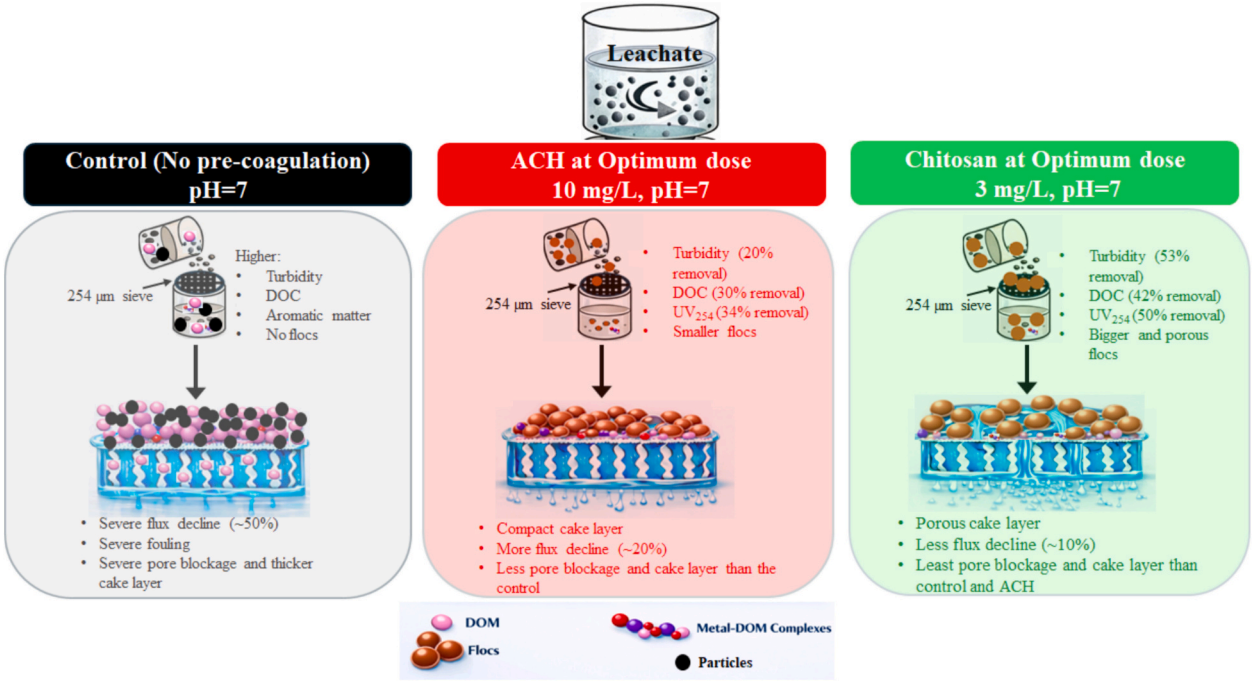

Fig. 7. Conceptual illustration of coagulant-specific fouling mitigation mechanisms.

Table 2
Effect of pre-coagulation with ACH and chitosan on UF fouling model parameters.

ACH							
Dose (mg/L)	**Model fit (R^2)**	**RMSE**	**SEE**	**SSE**	**K_c (s/m^2)**	**K_s (1/m)**	**K_cJ_o/K_s**
0	0.99	0.0026	0.0032	$5.22*10^{-5}$	17,335	1.37	2.71
5	0.99	0.0044	0.0062	$1.14*10^{-4}$	6676	0.67	2.25
10	0.99	0.0062	0.0088	$2.34*10^{-4}$	2798	0.26	2.24
20	0.99	0.0040	0.0052	$1.09*10^{-4}$	9326	0.80	2.63
30	0.99	0.0032	0.0040	$8.10*10^{-5}$	16,267	1.07	3.41
Chitosan							
0	0.99	0.0026	0.0032	$5.22*10^{-5}$	17,335	1.37	2.71
1	0.98	0.0049	0.0065	$1.68*10^{-4}$	7343	0.61	2.68
3	0.99	0.0029	0.0045	$4.11*10^{-5}$	1559	0.15	2.34
5	0.99	0.0042	0.0059	$1.05*10^{-4}$	1704	0.14	2.69

treated water decreased to ~3.25 L/mg·m, indicating relative enrichment of less aromatic, more hydrophilic DOM fractions in the treated water. These residual DOM fractions, together with retained metal species, may contribute to persistent organic–inorganic fouling. In addition, the presence of Si and O on the fouled membrane surface suggests deposition of silica or silicate-related particles originating from soil minerals, which may further contribute to compact fouling layers and irreversible hydraulic resistance. However, the extent to which the irreversible fouling arises from specific metal–DOM complexes cannot be conclusively resolved using the current dataset. Advanced molecular-level techniques, such as Fourier transform ion cyclotron resonance mass spectrometry (FT-ICR-MS), LC-ICP-MS-ESI-MS, or Orbitrap-based LC-MS, are needed to directly elucidate these complexation mechanisms and will be pursued in future work [90–93].

Overall, these results demonstrate that chitosan mitigates membrane fouling more effectively than ACH by promoting the formation of large, porous flocs via polymer bridging, thereby reducing pore blockage and cake layer resistance. While irreversible fouling associated with metal–DOM complexation cannot be fully eliminated, chitosan offers a mechanistically distinct and more effective pathway for fouling control in inline coagulation–ultrafiltration systems.

3.5. UF permeate water quality and surrogate DBP precursor indicators

UF permeate water quality was evaluated using turbidity, DOC, and UV254 to assess the combined effectiveness of pre-coagulation and ultrafiltration in reducing particulate matter, DOM, and surrogate indicators of DBP precursor loading (Fig. 8 and Fig. S11, Supplementary Information). Because DBP formation potential, including THMs and HAAs, was not directly measured in this study, the discussion focuses on DOC, UV_{254}, and humic−/fulvic-like fluorescence as surrogate indicators rather than direct measures of DBP formation. Under all tested conditions, particulate matter was effectively removed by the UF membrane; therefore, the following discussion focuses primarily on DOM fractions associated with potential DBP precursors. At the optimal ACH dose (10 mg/L), permeate DOC decreased to approximately 1.5 mg/L, corresponding to ~40% rejection, while UV_{254} was reduced to ~0.05 cm^{-1} (50% rejection). In contrast, chitosan pre-coagulation at its optimal dose (3 mg/L) resulted in substantially improved permeate quality. Permeate DOC was reduced to 1.0 mg/L^{-1} (60% rejection, paired *t*-test, p = 0.002), and UV_{254} declined to 0.03 cm^{-1} (70% rejection, paired t-test, p = 0.053). The disproportionately greater reduction in UV_{254} relative to DOC indicates preferential removal of aromatic, humic and fulvic-like DOM (Fig. S11, Supplementary Information), which are commonly associated with DBP formation potential [53,69,70]. This enhanced selectivity is consistent with chitosan's combined charge neutralization and polymer-bridging mechanisms, which promote aggregation and upstream removal of potential DBP precursors while simultaneously mitigating membrane fouling. Moreover, the performance of the present study, specifically in terms of DOC removal, was compared with previous studies employing hybrid coagulation–UF processes using different coagulants. Chitosan achieved comparable or higher DOC removal than many reported coagulants, even at a substantially lower dose, as summarized in Table S1 in the Supplementary Information.

Collectively, these results demonstrate that chitosan pre-coagulation provides multiple treatment benefits at substantially lower dosages than ACH. The higher removal efficiency achieved prior to membrane filtration reduces solids loading to the UF system, thereby improving hydraulic performance and operational robustness. During UF operation, membrane fouling is more effectively controlled, surrogate DBP precursors indicators are reduced, and higher-quality permeate is produced prior to subsequent disinfection. Moreover, the lower optimal dose of chitosan is expected to reduce sludge production relative to ACH [47], and the resulting organic-rich sludge may offer opportunities for beneficial reuse, such as soil amendment [76]. Although chitosan is generally more expensive per unit mass than aluminum-based coagulants, its lower effective dose and improved fouling control suggest that cost should be evaluated on a dose-normalized and performance-normalized basis. In addition to chemical cost, future techno-economic and life-cycle analyses should consider fouling-related energy demand, cleaning frequency, membrane lifetime, sludge production, and sludge disposal or reuse options.

Table 3
Effect of pH on fitted parameters of the combined standard pore-blocking and cake filtration model for chitosan pre-coagulation.

pH	Model fit (R^2)	RMSE	SEE	SSE	K_c (s/m^2)	K_s (1/m)	K_cJ_o/K_s
7	0.99	0.0029	0.0042	$4.11*10^{-5}$	1559	0.15	2.34
6	0.99	0.0028	0.0037	$5.58*10^{-5}$	9202	0.73	2.69
5	0.99	0.0024	0.0032	$4.15*10^{-5}$	10,085	0.72	2.97

Table 4
EDS analysis of the pristine and fouled membranes after backwash.

	Elemental composition (%)						
	C	**F**	**O**	**N**	**Al**	**Si**	**Fe**
Pristine	48.8	47.9	3.2	N/A	N/A	N/A	N/A
Control	12.9	12.0	43.5	N/A	10.9	19.0	1.7
10 mg/L ACH, pH 7	9.6	9.7	44.9	N/A	16.6	17.0	2.2
3 mg/L chitosan, pH 7	11.2	9.8	45.7	N/A	13.9	15.8	3.6
3 mg/L chitosan, pH 6	6.1	N/A	56.8	1.1	11.6	19.7	4.7
3 mg/L chitosan, pH 5	4.9	N/A	56.2	1.9	14.0	19.7	3.3

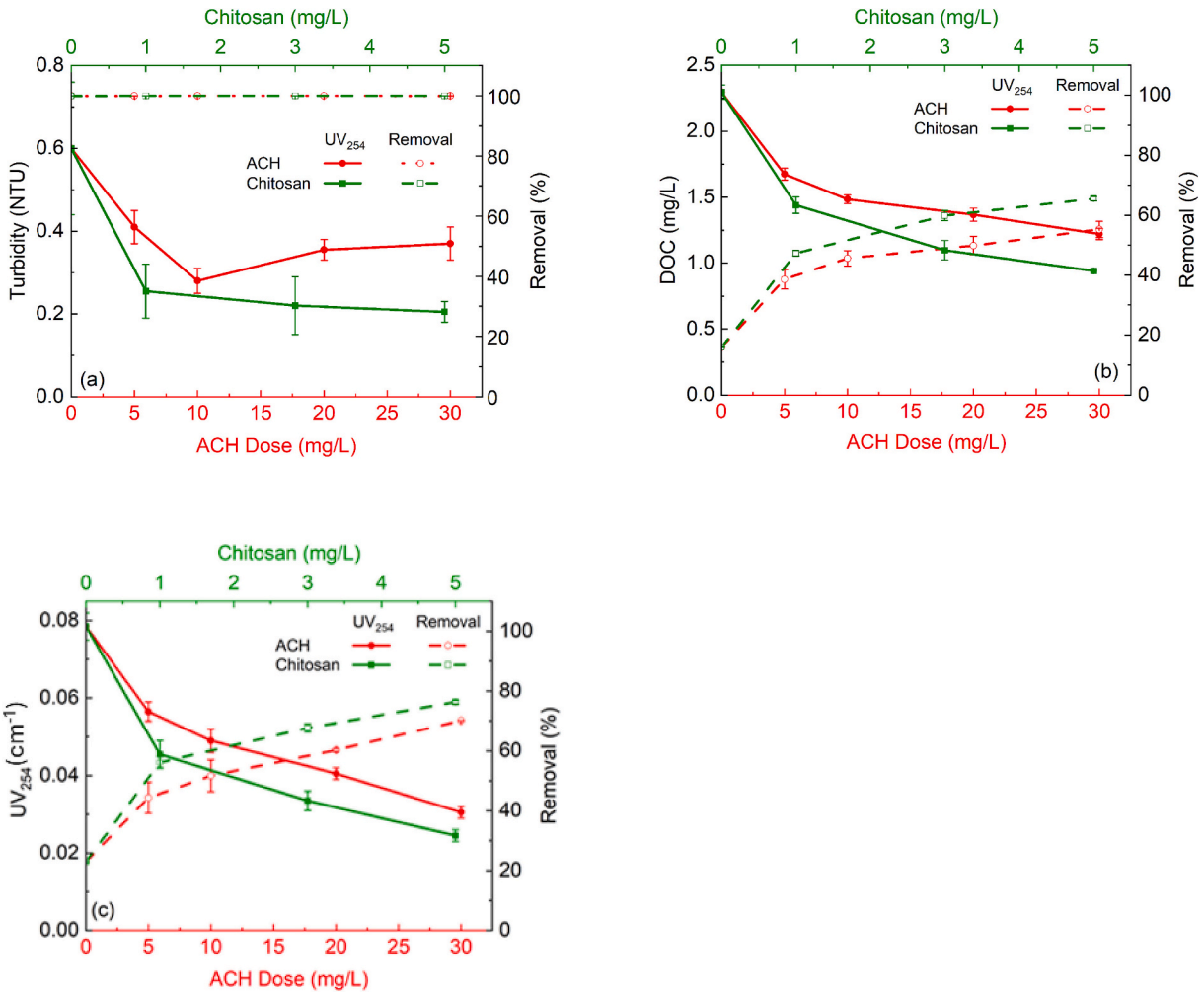

Fig. 8. UF permeate water quality as a function of coagulant type and dose: (a) turbidity, (b) DOC, and (c) UV_{254} (pH = 7).

Short-term dead-end UF experiments were used in this study to provide a controlled comparison of coagulant effects on immediate fouling behavior. However, this configuration does not fully represent full-scale cross-flow or submerged membrane systems, where hydrodynamic shear, air scouring, periodic backwashing, hydraulic relaxation, and chemically enhanced cleaning can substantially influence foulant deposition and removal. In long-term operation, residual chitosan may also interact with membrane surfaces or accumulated foulant layers, potentially affecting cleaning efficiency, fouling reversibility, and operational stability. Therefore, future studies should evaluate chitosan-assisted pre-coagulation under extended filtration–backwash cycles using cross-flow or submerged UF systems and wildfire-affected source waters collected across burn-severity gradients and seasonal hydrologic conditions.

4. Conclusions

Our study provided a comparison of ACH and chitosan as pre-coagulants for inline coagulation–ultrafiltration treatment of a wildfire-affected soil leachate, with emphasis on coagulation performance, membrane fouling mitigation, permeate water quality, and fouling mechanisms. The key findings are summarized as follows:

1. Without pre-coagulation, both reversible and irreversible membrane fouling were severe due to the extremely high turbidity, moderate DOC concentration and aromatic organic matter (UV_{254}), including fulvic- and humic-like DOM, present in the wildfire-impacted leachate. These characteristics led to rapid flux decline driven by initial pore blockage followed by cake layer formation.
2. Chitosan outperformed ACH at a much lower optimal dose (3 mg/L for chitosan vs. 10 mg/L for ACH). Through combined charge neutralization and polymer-bridging mechanisms, chitosan achieved greater removal of turbidity, DOC, and UV_{254} prior to ultrafiltration and produced flocs that formed earlier, were larger, and exhibited higher porosity. These flocs functioned as an effective dynamic pre-filter, resulting in slower flux decline and reduced pore-blockage and cake-layer resistances compared to ACH. Enhanced upstream removal translated to superior UF permeate quality, with greater rejection of DOC and UV_{254}, indicating preferential removal of aromatic, humic-like DOM often associated with DBP precursor characteristics.
3. Chitosan performance was strongly pH dependent. While DOC and UV_{254} removal were maximized near pH 6 due to increased amine protonation, fouling mitigation was most effective at neutral pH. At lower pH, excessive adsorption of protonated chitosan onto the negatively charged PVDF membrane led to dense, hydrated fouling layers and increased fouling resistance, as confirmed by comprehensive membrane characterization.

Overall, our work demonstrated that chitosan was a mechanistically distinct and more effective alternative to conventional aluminum-based coagulants for inline coagulation–UF treatment of water that may have had similar characteristics to natural source waters from recently burned areas following large precipitation events. Although irreversible fouling

associated with residual metal–DOM interactions could not be fully eliminated, chitosan reduced pore blockage and cake-layer resistance through favorable floc formation. Future research should evaluate long-term performance under cross-flow or submerged UF configurations and apply advanced molecular-level analytical tools to further elucidate metal–DOM complexation mechanisms governing irreversible fouling.

Declaration of competing interest

The authors declare that they have no known competing financial interests or personal relationships that could have appeared to influence the work reported in this paper.

Acknowledgements

This work was supported by the U.S. Forest Service under Agreements No. 22-JV-11261952-071 and 23-JV-11261954-057. The authors acknowledge Prof. Stacey Harper for providing access to the Zetasizer nanoseries (Malvern Instruments) and Prof. Yanyun Zhao for supplying the chitosan used in this study. Professor Adam Z. Higgins (OSU CBEE) for providing access to the microscope instrument, and FTIR analysis was performed at the Oregon Process Innovation Center, part of the Northwest Nanotechnology Infrastructure (NNCI) at Oregon State University, supported in part by the National Science Foundation (Grant No. NNCI-2025489) and Oregon State University. We thank Weyerhaeuser Company for site access to collect field samples.

Appendix A. Supplementary data

Supplementary data to this article can be found online at https://doi.org/10.1016/j.seppur.2026.138996.

Data availability

Data will be made available on request.

References

[1] R. Costanza, et al., The value of the world's ecosystem services and natural capital, Nature 387 (6630) (1997) 253–260.
[2] S.M. Stein, Forests on the edge: housing development on America's private forests 636, US Department of Agriculture, Forest Service, Pacific Northwest Research Station, 2005.
[3] H.G. Smith, et al., Wildfire effects on water quality in forest catchments: a review with implications for water supply, J. Hydrol. 396 (1–2) (2011) 170–192.
[4] C. Santín, et al., Quantity, composition and water contamination potential of ash produced under different wildfire severities, Environ. Res. 142 (2015) 297–308.
[5] A. Vergnoux, et al., Effects of forest fires on water extractable organic matter and humic substances from Mediterranean soils: UV–vis and fluorescence spectroscopy approaches, Geoderma 160 (3–4) (2011) 434–443.
[6] J.-J. Wang, et al., Temporal variations of disinfection byproduct precursors in wildfire detritus, Water Res. 99 (2016) 66–73.
[7] B.R. Goforth, et al., Spatial distribution and properties of ash and thermally altered soils after high-severity forest fire, southern California, Int. J. Wildland Fire 14 (4) (2005) 343–354.
[8] E.C. Oliveira-Filho, et al., Effects of ashes from a Brazilian savanna wildfire on water, soil and biota: an ecotoxicological approach, Sci. Total Environ. 618 (2018) 101–111.
[9] S.E. Ryan, K.A. Dwire, M.K. Dixon, Impacts of wildfire on runoff and sediment loads at little Granite Creek, western Wyoming, Geomorphology 129 (1–2) (2011) 113–130.
[10] G.W. Minshall, C.T. Robinson, D.E. Lawrence, Postfire responses of lotic ecosystems in Yellowstone National Park, USA, Can. J. Fish. Aquat. Sci. 54 (11) (1997) 2509–2525.
[11] G.A. Akie, et al., An intercomparison of DOC estimated from fDOM sensors in wildfire affected streams of the western United States, Hydrol. Process. 38 (12) (2024) e70023.
[12] S. Wall, et al., Post-wildfire water quality and aquatic ecosystem response in the US Pacific Northwest: science and monitoring gaps, Environ. Res. Water 2 (1) (2026) 015004.
[13] K.A. Wampler, K.D. Bladon, A.N.J.B. Myers-Pigg, The influence of burn severity on dissolved organic carbon concentrations across a stream network differs based on seasonal wetness conditions, Biogeosciences 21 (13) (2024) 3093–3120.
[14] K. Wampler, et al., Spatial and temporal shifts in dissolved organic matter character across a burned stream network, J. Geophys. Res. Biogeosci. 130 (7) (2025) e2024JG008687.
[15] J.A. Roebuck Jr., et al., Molecular shifts in dissolved organic matter along a burn severity continuum for common land cover types in the Pacific northwest, USA, Sci. Total Environ. 958 (2025) 178040.
[16] L.J. Magliozzi, et al., Wildland–urban interface wildfire increases metal contributions to stormwater runoff in Paradise, California, Environ Sci Process Impacts 26 (4) (2024) 667–685.
[17] S.R. Earl, D.W. Blinn, Effects of wildfire ash on water chemistry and biota in South-Western USA streams, Freshw. Biol. 48 (6) (2003) 1015–1030.
[18] M.T. Beyene, et al., To burn or not to burn: an empirical assessment of the impacts of wildfires and prescribed fires on trace element concentrations in Western US streams, Sci. Total Environ. 863 (2023) 160731.
[19] P.J. Robichaud, J.C. Padowski, Drinking water under fire: water utilities' vulnerability to wildfires in the Pacific northwest, JAWRA J. Am. Water Res. Assoc. 60 (2) (2024) 590–602.
[20] E.J. Davis, S.J.a.B.J., Community Drinking Water Systems in Oregon Trees to Tap: How Forest Practices Affect Oregon's Municipal Water, Oregon State University Extension Service, 2021, pp. 16–51, available at, https://extension.oregonstate.edu/catalog/pub/em-9295-trees-tap-how-forest-practices-affect-oregons-municipal-water.
[21] J.C. Padowski, Assessing the need for fire-related decision-support tools for water management in the Pacific Northwest, USA, Washington State Univeristy, 2021. https://s3.wp.wsu.edu/uploads/sites/95/2021/09/Surve ySummary_Final.pdf.
[22] A.K. Hohner, et al., Wildfires alter forest watersheds and threaten drinking water quality, Acc. Chem. Res. 52 (5) (2019) 1234–1244.
[23] H. Huang, K. Schwab, J.G. Jacangelo, Pretreatment for low pressure membranes in water treatment: a review, Environ. Sci. Technol. 43 (9) (2009) 3011–3019.
[24] S. Nakatsuka, I. Nakate, T. Miyano, Drinking water treatment by using ultrafiltration hollow fiber membranes, Desalination 106 (1–3) (1996) 55–61.
[25] D. Xu, et al., A comparison study of sand filtration and ultrafiltration in drinking water treatment: removal of organic foulants and disinfection by-product formation, Sci. Total Environ. 691 (2019) 322–331.
[26] A. Zularisam, et al., Application of coagulation–ultrafiltration hybrid process for drinking water treatment: optimization of operating conditions using experimental design, Sep. Purif. Technol. 65 (2) (2009) 193–210.
[27] H. Shon, et al., Fouling of ultrafiltration membrane by effluent organic matter: a detailed characterization using different organic fractions in wastewater, J. Membr. Sci. 278 (1–2) (2006) 232–238.
[28] A. Zularisam, et al., The effects of natural organic matter (NOM) fractions on fouling characteristics and flux recovery of ultrafiltration membranes, Desalination 212 (1–3) (2007) 191–208.
[29] J.P. VanderRoest, et al., Fire impacts on the soil metabolome and organic matter biodegradability, Environ. Sci. Technol. 58 (9) (2024) 4167–4180.
[30] R. Kumar, A. Ismail, Fouling control on microfiltration/ultrafiltration membranes: effects of morphology, hydrophilicity, and charge, J. Appl. Polym. Sci. 132 (21) (2015).
[31] H. Xu, et al., Dissolved organic matters with low molecular weight fractions exhibit high photochemical potential for reactive oxygen formation, Chemosphere 305 (2022) 135542.
[32] X. Zhang, et al., Anti-fouling mechanism of ultrafiltration membranes modified by graphene oxide with different charged groups under simulated seawater conditions, J. Membr. Sci. 674 (2023) 121483.
[33] Y.-H. Cheng, et al., Surface modification of ultrafiltration membranes with 1, 4-benzoquinone and polyetheramines to improve fouling resistance, ACS Appl. Mater. Interfaces 14 (46) (2022) 52390–52401.
[34] W. Yu, et al., Ultrafiltration and nanofiltration membrane fouling by natural organic matter: mechanisms and mitigation by pre-ozonation and pH, Water Res. 139 (2018) 353–362.
[35] G. Veréb, et al., Effects of pre-ozonation on membrane filtration of oil-in-water emulsions using different polymeric (PES, PAN, PTFE) ultrafilter membranes, Ozone Sci. Eng. 42 (3) (2020) 230–243.
[36] G.-Y. Kim, et al., Pretreatment strategies for mitigation of membrane fouling by effluent organic matter in ultrafiltration: ozonation and coagulation/flocculation, Desalin. Water Treat. 77 (2017) 177–184.
[37] J. Zhu, Wei Xu, Yuwei Yang, Xiaomei Su, Xiao Xiao, Feng dong, Hailu fu, Chongjun Chen, Jianrong Chen, Faqian sun, Quorum quenching driven microbial community to biofouling control in membrane bioreactor for landfill leachate treatment, J. Membr. Sci. 722 (2025) 123899.
[38] S. Farooq, et al., Treatment of burned soil leachates by ultrafiltration coupled with coagulation: insights into membrane fouling, Water Res X 28 (2025) 100357.
[39] Q.N. Tran, X. Jin, N.Q. Doan, Enhanced removal of extracellular microcystin-LR using chitosan coagulation-ultrafiltration: performance and mechanisms, J. Environ. Chem. Eng. 10 (3) (2022) 107902.
[40] S. Kawamura, Effectiveness of natural polyelectrolytes in water treatment, J. Am. Water Works Assoc. 83 (10) (1991) 88–91.
[41] H. Xin, et al., Mechanisms and performance of calcium peroxide-enhanced Fe (II) coagulation for treatment of *Microcystis aeruginosa*-laden water, Environ. Sci.: Water Res. Technol. 6 (5) (2020) 1272–1285.
[42] D. Zhang, et al., Influence of coagulation process on the ultrafiltration performance–the roles of Al species and characteristics of algae-laden water, Sep. Purif. Technol. 183 (2017) 32–42.
[43] Y. Zhang, et al., The change of NOM in a submerged UF membrane with three different pretreatment processes compared to an individual UF membrane, Desalination 360 (2015) 118–129.

[44] P. Niquette, et al., Impacts of substituting aluminum-based coagulants in drinking water treatment, Water Quality Res. J. 39 (3) (2004) 303–310.
[45] F. Renault, et al., Chitosan for coagulation/flocculation processes–an eco-friendly approach, Eur. Polym. J. 45 (5) (2009) 1337–1348.
[46] F. Rassaei, Chitosan as an organic amendment to improve soil properties and plant growth in the presence of polystyrene microplastics, Environ. Prog. Sustain. Energ. 43 (2) (2024) e14301.
[47] Q.N. Tran, D. Mason, X. Jin, Impact of chitosan molecular weight on coagulation efficiency and membrane fouling alleviation in microcystis aeruginosa-impacted water treatment, J. Water Process Eng. 76 (2025) 108265.
[48] EPA, U, Enhanced coagulation and enhanced precipitative softening guidance manual. Disinfectants and disinfection byproducts rule (DBPR), 1999.
[49] USEPA, Stage 1 Disinfectants and Disinfection Byproducts Rule Office of Water and Drinking Ground Water, Washington, DC, 2001.
[50] USEPA, Enhanced Coagulation and Enhanced Precipitative Softening Guidance Manual. Office of Water and Drinking Ground Water, Washington, DC, 1998.
[51] Y. Deng, et al., A universal model to predict DOC removal by coagulation based on UV-visible absorption spectrum, Water Res. 286 (2025) 124160.
[52] H. Cui, et al., Application progress of enhanced coagulation in water treatment, RSC Adv. 10 (34) (2020) 20231–20244.
[53] S. Tak, B.P. Vellanki, Natural organic matter as precursor to disinfection byproducts and its removal using conventional and advanced processes: state of the art review, J. Water Health 16 (5) (2018) 681–703.
[54] H. Uzun, et al., Two years of post-wildfire impacts on dissolved organic matter, nitrogen, and precursors of disinfection by-products in California stream waters, Water Res. 181 (2020) 115891.
[55] USGS, U.F.S., MTBS data access: fire level geospatial data, MTBS Project, 2026.
[56] H.E. Beck, et al., Present and future Köppen-Geiger climate classification maps at 1-km resolution, Sci. Data 5 (1) (2018) 180214.
[57] PRISM Group, O.S.U. https://prism.oregonstate.edu, 2026.
[58] Soil Survey Staff, Natural Resources Conservation Service, United States Department of Agriculture. Soil survey geographic (SSURGO) Database. *https://sdmdataaccess.sc.egov.usda.gov*, 2026.
[59] BAER Imagery Support Program, Geospatial technology and applications Center, USDA Forest Service. *https://fsapps.nwcg.gov/afm/baer/download.php?year=2023*, 2026.
[60] G. Bolton, D. LaCasse, R. Kuriyel, Combined models of membrane fouling: development and application to microfiltration and ultrafiltration of biological fluids, J. Membr. Sci. 277 (1–2) (2006) 75–84.
[61] S. Abi Farraj, et al., Microplastics and Nanoplastics in Water: Improving Removal in Wastewater Treatment Plants with Alternative Coagulants, 2026.
[62] C.N. Dahm, et al., Extreme water quality degradation following a catastrophic forest fire, Freshw. Biol. 60 (12) (2015) 2584–2599.
[63] J.H. Writer, et al., Water treatment implications after the high park wildfire, Colorado 106 (4) (2014) E189–E199.
[64] C.H. Sham, M.E. Tuccillo, J. Rooke, Effects of wildfire on drinking water utilities and best practices for wildfire risk reduction and mitigation, 4482, Water Research Foundation, Denver, CO, 2013.
[65] S. Zhu, et al., Influences of wildfire on the soil dissolved organic matter characteristics and its electron-donating capacity, Water Res. 266 (2024) 122382.
[66] S.J. Fischer, et al., Fluorescence and absorbance indices for dissolved organic matter from wildfire ash and burned watersheds, ACS EST Water 3 (8) (2023) 2199–2209.
[67] W. Wang, et al., Purification, characterization and application of dual coagulants containing chitosan and different Al species in coagulation and ultrafiltration process, J. Environ. Sci. 51 (2017) 214–221.
[68] P. Du, et al., Optimized coagulation pretreatment alleviates ultrafiltration membrane fouling: the role of floc properties and slow-mixing speed on mechanisms of chitosan-assisted coagulation, J. Environ. Sci. 82 (2019) 82–92.
[69] R.S. Summers, et al., Assessing DBP yield: uniform formation conditions, J. Am. Water Works Assoc. 88 (6) (1996) 80–93.
[70] D.D. Gang, et al., Using chlorine demand to predict TTHM and HAA9 formation, J. Am. Water Works Assoc. 94 (10) (2002) 76–86.
[71] Y. Chen, et al., Assessment of the chlorine demand and disinfection byproduct formation potential of surface waters via satellite remote sensing, Water Res. 165 (2019) 115001.
[72] A. Abdelrasoul, H. Doan, A. Lohi, Fouling in Membrane Filtration and Remediation Methods, in: Mass Transfer-Advances in Sustainable Energy and Environment Oriented Numerical Modeling, 2013.
[73] Z.-y. Yuan, et al., Identifying key residual aluminum species responsible for aggravation of nanofiltration membrane fouling in drinking water treatment, J. Membr. Sci. 659 (2022) 120833.
[74] A.H. Behroozi, et al., Engineered chitosan for water purification: mechanistic insights and material innovations for contaminant removal, Carbohydr. Polym. 375 (2025) 124757.
[75] Q.Z. Wang, et al., Protonation constants of chitosan with different molecular weight and degree of deacetylation, Carbohydr. Polym. 65 (2) (2006) 194–201.
[76] L.A. Picos-Corrales, et al., Chitosan as an outstanding polysaccharide improving health-commodities of humans and environmental protection, Polymers 15 (3) (2023) 526.
[77] S.B. Kurniawan, et al., Challenges and opportunities of biocoagulant/bioflocculant application for drinking water and wastewater treatment and its potential for sludge recovery, Int. J. Environ. Res. Public Health 17 (24) (2020) 9312.
[78] T. Fujioka, et al., Controlling membrane fouling of nanofiltration using poly-aluminum chloride and Moringa oleifera coagulants, Sep. Purif. Technol. 334 (2024) 126016.
[79] D. Toloman, et al., Photocatalytic self-cleaning PVDF membrane blended with MWCNT-ZnO nanocomposites for RhB removal, Coatings 13 (3) (2023) 594.
[80] Z. Zeng, et al., Graphene oxide quantum dots covalently functionalized PVDF membrane with significantly-enhanced bactericidal and antibiofouling performances, Sci. Rep. 6 (1) (2016) 20142.
[81] H.-K. Lee, S.-J. Choi, Copper ferrocyanide chemically immobilized onto a polyvinylidene fluoride hollow-fibre membrane surface for the removal of aqueous cesium, Environ. Technol. 43 (15) (2022) 2241–2251.
[82] Y. Hao, et al., Effect of metal ions on the protein fouling of hollow-fiber ultrafiltration membranes, Sep. Purif. Technol. 111 (2013) 137–144.
[83] J.K. Edzwald, W.C. Becker, K.L. Wattier, Surrogate parameters for monitoring organic matter and THM precursors, J. Am. Water Works Assoc. 77 (4) (1985) 122–132.
[84] W. Yuan, A.L. Zydney, Humic acid fouling during ultrafiltration, Environ. Sci. Technol. 34 (23) (2000) 5043–5050.
[85] F. Xiao, et al., Identification of key factors affecting the organic fouling on low-pressure ultrafiltration membranes, J. Membr. Sci. 447 (2013) 144–152.
[86] P. Merdy, et al., Evidence of humic acid-aluminium-silicon complexes under controlled conditions, Sci. Total Environ. 829 (2022) 154601.
[87] S. Kügler, et al., Iron-organic matter complexes accelerate microbial iron cycling in an iron-rich fen, Sci. Total Environ. 646 (2019) 972–988.
[88] X. Zhang, et al., Effects of Ca2+ and Mg2+ on Cu binding in hydrophilic and hydrophobic dissolved organic matter fractions extracted from agricultural soil, Chemosphere 352 (2024) 141441.
[89] I. Fernández, et al., Organic matter changes immediately after a wildfire in an Atlantic forest soil and comparison with laboratory soil heating, Soil Biol. Biochem. 29 (1) (1997) 1–11.
[90] L. Nyarko, et al., Tracking changes in organic-copper speciation during wastewater treatment using LC-ICPMS-ESIMS, ACS Environ. Au 5 (2) (2025) 230–240.
[91] Y. He, et al., Unraveling the characteristics of dissolved organic matter removed by aluminum species based on FT-ICR MS analysis, Water Res. 255 (2024) 121429.
[92] J. Lv, et al., Molecular-scale investigation with ESI-FT-ICR-MS on fractionation of dissolved organic matter induced by adsorption on iron oxyhydroxides, Environ. Sci. Technol. 50 (5) (2016) 2328–2336.
[93] Q. Pan, et al., Validation and evaluation of high-resolution orbitrap mass spectrometry on molecular characterization of dissolved organic matter, ACS Omega 5 (10) (2020) 5372–5379.